Budoor M. Saleh
Mohanad Q. Kareem

Departments of Physics,
College of Science,
University of Kirkuk,
Kirkuk, IRAQ

Morphology-Engineered $CuBiS_2$ Thin Films for Next-Generation Dual-Gas Sensors

In this research, we will present a description in detailed of $CuBiS_2$ composite films fabricated via a thermal solvent approach for dual gas sensing applications, targeting H_2S and NO_2 gases. The films were systematically analyzed and the results show that the $CuBiS_2$ films exhibit various advantages such as excellent gas sensing, with excellent performance controlled by operating temperature, film thickness, and surface morphology. The formation of metal-sulfur bonds was revealed and a wide direct band gap of 3.84 eV was determined. Electrical evaluations confirm the p-type conductivity, suggesting their potential application in thermoelectric devices. The membranes exhibit increased sensitivity to H_2S and NO_2 at high temperatures, confirming their potential application in environmental monitoring and industrial safety applications. This research suggests the importance of further optimizing the membrane composition and structural properties to develop sensitivity and selectivity, which will assist in the development of cost-effective and reliable gas sensors in the field of nanomaterials.

***Keywords*:** $CuBiS_2$; Gas sensors; Thioglycolic acid (TGA); Thermal solvent approach
Received: 04 December 2024; **Revised:** 12 February 2025; **Accepted:** 17 February 2025

1. Introduction

There are a lot of applications to enumerate, including monitoring environmental pollution, industrial process control, and public health. The detection of toxic gases like H_2S and NO_2 is very critical owing to their toxicity and contribution to environmental damage. Recent developments in material chemistry have experienced the development of some new sensing materials. Amongst these, ternary chalcogenide compounds such as copper bismuth sulfide ($CuBiS_2$) seem to be a promising candidate for gas sensor applications. H_2S is a colorless, flammable gas with a characteristic rotten egg odor, and exposure to it, even at small concentrations, is severely hazardous to health. The health effects of H_2S include irritation to the respiratory system, headaches, and in extreme instances, loss of consciousness and even death [1]. The other sources of emission of H_2S include industrial processes related to the refining of oil and gas, wastewater treatment, and paper manufacture, which demands by the use of an efficient gas-detecting system [2]. NO_2, or in its chemical terminology, nitrogen dioxide, is a reddish-brown-colored gas with a pungent, acrid smell and it is one of the most important air pollutants participating in the formation of smog and acid rain. Vehicle and industrial processes are the main source of NO_2 production. The final result is respiratory problems and susceptibility to respiratory infection with long-term exposure to NO_2 [3]. The World Health Organization has mandatory strict limits on NO_2 exposure, which enforces huge demands on detection techniques for high sensitivity and precision [4]. Traditional gas sensor technologies very often rely on the use of metal oxide semiconductors, which feature some disadvantages regarding high power consumption, limited selectivity or poor long-term stability [5]. This has spurred investigations into other materials that can provide superior performance and greater versatility. $CuBiS_2$ represents a p-type semiconductor, which has an interesting crystal structure with layers. It attracted much attention due to its unique electronic properties and its proposed gas sensitivity. In neoteric years, considerable progress was performed in the development of composite thin films for use in gas sensors. To optimize this material for sensor applications [6], a wide variety of synthesis methods have been tried. Various techniques exist for the synthesis of these materials. One of the most used is the solvothermal approach, in which particle size and morphology control effectively and composition [7] also precisely. Normally, this technique involves the reaction of precursor salts under controlled temperature and pressure conditions in a sealed autoclave. Besides, several physical depositions tried to prepare $CuBiS_2$ thin films by various techniques like thermal evaporation and sputtering techniques [8]. These methods provide excellent control of film thickness and uniformity but require high-temperature post-deposition annealing to improve crystallinity. Among the chemical deposition methods are spray pyrolysis and chemical bath deposition techniques that have been reported as cost-effective alternatives for $CuBiS_2$ film large-area deposition [9]. The structural parameters of $CuBiS_2$ are of vital importance in its application in gas sensing. It crystallizes in an orthorhombic structure and has a layered arrangement of Cu-S and Bi-S polyhedral [10]. Because of this, the layered nature could promote intercalation of gas molecules across its surfaces, thus improving the sensing response. From XRD studies, it is found that

the crystallinity and preferred orientation of $CuBiS_2$ films can be modified with variation of synthesis parameters and hence their sensing characteristics [11]. The $CuBiS_2$ thin films are characterized by strong absorption in the visible and near-infrared region. $CuBiS_2$ possesses a direct bandgap between 1.3-1.6 eV, hence, this material is suitable for different optoelectronic applications apart from gas sensing [12]. UV-visible spectroscopy and photoluminescence studies gave an idea about the electronic structure and defect states in $CuBiS_2$, which is crucial for the understanding of interaction of $CuBiS_2$ with gas molecule [13]. Electrical characterization of $CuBiS_2$ thin films shows p-type conductivity, with carrier concentrations in the range of 10^{16}-10^{18} cm^{-3} [14]. Electrical properties can be tuned by varying the Cu:Bi ratio and doping incorporated. Hall effect measurements and studies based on temperature dependence of conductivity have explained charge transport mechanisms in $CuBiS_2$, which are intrinsic for its gas-sensing behavior [15]. Up to now, $CuBiS_2$ composite thin films have shown promising applications in the aspect of gas sensing. Sensitivities towards reducing gases like H_2S and oxidizing gases such as NO_2 have been observed [16]. The sensing mechanism usually is ascribed to changes in electrical resistance due to gas adsorption on the surface of the film. Operating temperature, film thickness, and surface morphology are some of the major parameters affecting performance [17]. The shape and size of nano-$CuBiS_2$ are a very important concern in determining the gas sensing properties. A variety of shapes such as nanoparticles, nanosheets, and hierarchical structures have been synthesized to enhance the surface area with improvements in gas-solid interactions. Most of these nanostructures exhibit enhanced sensitivity and response times compared to bulk films. Further research has gone into improving the selectivity and stability of the $CuBiS_2$-based gas sensors. Such strategies include surface functionalization, noble metal decoration, and the formation of heterostructures with other semiconducting materials to improve sensor performance [18]. In addition, recent efforts to integrate $CuBiS_2$ thin films into MEMS platforms have provided new opportunities toward miniaturized, low-power gas detection devices [19]. Composite $CuBiS_2$ thin films represent an exciting material system for next-generation gas sensors, particularly for hydrogen sulfide and nitrogen dioxide detection [20]. With the possibility of tuning structural, optical, and electrical properties by different synthesis and processing techniques, this material provides a promising versatile platform for sensor development [21]. Further research in the field will most probably establish the importance of sensors based on.

2. Experimental Work

The synthesis process begins with the specific gravity of the starting materials. A round-bottomed flask is loaded with 1.94 g of bismuth nitrate pentahydrate and 0.70 g of tin tetrachloride pentahydrate, both dissolved in 50 mL of dimethyl sulfoxide (DMSO) and stirred at room temperature for 30 min. At the same time, 0.4 g of polyvinylpyrrolidone (PVP) is dissolved in 30 ml of DMSO in another beaker, followed by stirring for 90 min. To this solution, 2 ml of thioglycolic acid is added and stirred for an additional 35 min. Afterward, 0.22 g of thiourea is introduced into the mixture and stirred using a magnetic stirrer for another 30 min. The resulting solution is then transferred to a Teflon-lined stainless steel pressure vessel, where previously cleaned glass substrates are placed vertically for uniform deposition. The vessel was sealed and maintained at 150°C for 6 h, followed by natural cooling to room temperature. After synthesis, the resulting films were heated in air at 300°C for 1 h to promote crystallization and eliminate residual organic compounds, thus improving the structural and functional properties of the films.

Substrate preparation was carefully ensured using distilled acetone and ensuring a surface free of impurities to allow the exit to swim. A hot-substrate deposition technique was used, where 2 ml of the compound solutions were well distributed on the substrates kept at 80°C. This method allows for a regenerative distribution of the material, which enhances the need for high-quality thin films. This process combines specialized precision with controlled reaction conditions, which ensures strict thin films with transparent compositional and structural properties.

The $CuBiS_2$ nanoparticles were analyzed using analytical techniques to determine their multiple properties, including shape, form, optical and electrical. X-ray diffraction (XRD) was performed using a Bruker Advance D8 device. Field-emission scanning electron microscopy (FE-SEM) and Energy-dispersive x-ray spectroscopy (EDS) were carried out using a TESCAN MIRA3 FE-SEM instrument. A Shimadzu UV-visible spectrophotometer was used to record absorption spectra of the prepared samples. The Fourier-transform infrared spectroscopy (FTIR) was performed to confirm the presence of functional groups and verification of the presence of the fundamental bonds. Electrical measurements were carried out to determine the conductivity and charge transfer behavior.

A specialized device evaluates Detection of H2S and NO2 at 30 ppm over temperatures up to 200 °C. It incorporates a robust detection approach including chamber evacuation, controlled gas introduction, and resistivity measurements. This thoughtful approach provides conclusive confirmation of the material's properties and expected applications. By carefully

changing the composition and structure during performance monitoring, researchers can develop the material for specific sensing or functional applications. The precise gas sensing procedures ensure reliable data for accurate evaluation of the material's sensing capabilities.

Clean glass pieces were heated to 80°C on a hot plate and using a small pipette, 2 ml of the prepared solution was gradually dropped onto the preheated substrate. The solution was left to spread evenly over the substrate surface while the substrate temperature was maintained at 80°C for 10 minutes to be sure uniform film formation. The substrate was removed from the hot plate and left to cool down the room temperature.

3. Results and Discussion

The XRD pattern of $CuBiS_2$ composite thin films is presented in Fig. (1) and table (1), accompanied by the corresponding JCPDS standard card no. 00-008-0086 for comparison. The pattern exhibits well-defined peaks, indicating the crystalline nature of the synthesized material. The most prominent peak appears at 2θ =19.984°, corresponding to the (-3,1,2) plane with 100% relative intensity. This peak aligns closely with the JCPDS standard, demonstrating a d -spacing of 3.05792 Å compared to the reference value of 3.07000 Å. Other significant peaks are observed at 2θ values of 15.428°, 23.582°, 28.697°, and 48.481°. The experimental d-spacing values show slight deviations from the JCPDS values, which can be attributed to lattice strain or compositional variations in the thin films. The full width at half maximum (FWHM) values range from 1.1625 to 3.0300, suggesting varying degrees of crystallite size and microstrain across different planes.

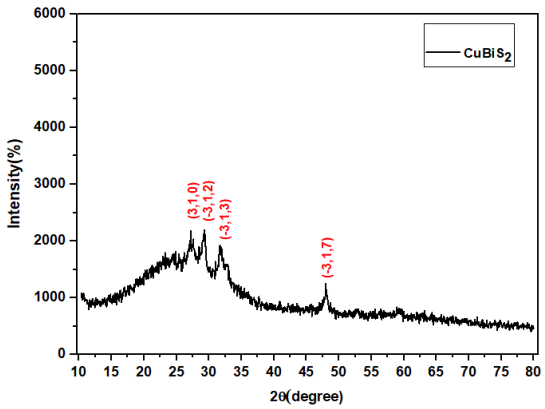

Fig. (1) XRD pattern of $CuBiS_2$ film prepared using Thioglycolic acid

The broadening due to small crystallite size may be expressed as [22]

$$\beta = \frac{k\lambda}{t\cos\theta} \quad (1)$$

The monoclinic crystal system of $CuBiS_2$ is confirmed by the indexing of the diffraction peaks, which match the JCPDS card. The presence of multiple peaks with varying intensities indicates the polycrystalline nature of the thin films. The relative intensities of the experimental peaks differ somewhat from the JCPDS standard, particularly for the (-3,1,3) and (-3,1,7) planes. This discrepancy may be due to preferred orientation effects in the thin film growth process or slight stoichiometric deviations in the synthesized material. The broadening of peaks, especially noticeable for the (2,1,0) reflection at 48.481°, suggests the presence of nanocrystalline domains within the thin film structure. This broadening can be quantitatively analyzed using the Scherrer equation to estimate crystallite sizes. In summary, XRD analysis confirms the successful synthesis of $CuBiS_2$ composite thin films exhibiting a monoclinic structure. These slight changes in peak position and intensity compared to the standard pattern give some clues about the microstructure of the film and the prospective further optimization of growth parameters respecting crystallinity and phase purity.

Figure (2) presents the FTIR spectrum of the $CuBiS_2$ thin film provides an in-depth insight into the molecular structure and chemical bonding in the material. The spectrum covers the region from 500 to 4000 cm^{-1} and shows several distinct absorption bands attributed to molecular vibrations in the complex structure. The broad, strong absorption band at 3376 cm^{-1} is attributed to O-H vibrations that may be due to water molecules adsorbed on the surface or hydroxyl groups present on the surface of the $CuBiS_2$ particles. The sharp peak at 1668 cm^{-1} shows that these vibrations are due to H-O-H bending, which supports the presence of water molecules in the sample, whether structural water or residual moisture from the synthesis process. In the characteristic part of the spectrum below 1500 cm^{-1}, several distinct peaks can be seen. The band at 1424 cm^{-1} may correspond to C-H bends that are likely due to organic residues or encapsulating agents used during the synthesis. The peak at 1014 cm^{-1} is attributed to vibrations Stretching of the S-O bond indicating partial surface oxidation of sulfur in the $CuBiS_2$ structure The sharp peak at 664 cm^{-1} undoubtedly arises from stretching vibrations of the M-S bond which is a direct evidence of the formation of Cu-S and Bi-S bonds within the host lattice of $CuBiS_2$ confirming the synthesis of the desired compound The thin film exhibits good optical transmission properties in the mid-IR region indicating the purity of the sample as shown in the table (2) which provides a brief overview of the main absorption bands as seen in the FTIR spectrum, their intensity and possible molecular assignments The IR spectral analysis provides essential information about the molecular structure and bonding in the $CuBiS_2$

thin films and confirms the formation of the desired metal-sulfur bonds while revealing the presence of adsorbed species on the surface which can guide the optimization of the synthesis process and inform potential applications of the material in areas such as solar energy or sensors.

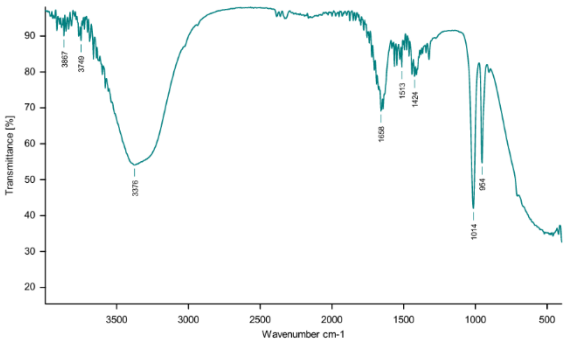

Fig. (2) FTIR spectrum of $CuBiS_2$ film prepared using Thioglycolic acid

Figure (3) presents a comprehensive analysis of $CuBiS_2$ composite thin films using FE-SEM and EDX. The FE-SEM images (3a and 3b) offer insights into the film's surface morphology and nanostructure. At 70.0kx magnification, the film exhibits a relatively smooth surface with scattered particulate features, suggesting a uniform deposition process with some localized aggregation. The high-magnification image at 350kx exhibits a finer resolution and gives an average particle size of 47.43 nm, which points toward the nanocrystalline nature of the film. EDX spectrum presented in Fig. (3c) confirms the elemental composition in $CuBiS_2$ thin film. The image that appears in the spectrum is composed of several elements. As expected, Copper (Cu) appears clearly in the spectrum, because it is an essential part of the $CuBiS_2$ compound. The Thioglycolic acid acts as a chelating agent that can coordinate copper in the solution, ensuring the formation of the $CuBiS_2$ compound regularly during the reaction. Sulfur (S) is the other essential element in $CuBiS_2$, and appears densely in the spectrum, as Thioglycolic acid contains sulfur (S-H group), making it an additional source of sulfur in the reaction and the solvent DMSO also contains sulfur (S=O group), which may contribute to the presence of sulfur in the spectrum. Bismuth (Bi) does not appear clearly in the spectrum, although it is an essential part of $CuBiS_2$. This may be due to the low x-ray sensitivity of bismuth under these conditions or its interference with other signals. Chlorine (Cl) in the spectrum can be interpreted as resulting from the addition of $SnCl_2$ during the preparation. Chlorine may remain in the sample as an impurity after the reaction or be deposited on the surface. Silicon (Si) can be either from the substrate on which the sample was placed or from external contamination. It is not directly related to thioglycolic acid or DMSO. Calcium (Ca) usually appears due to environmental contamination or from the equipment used during preparation. Oxygen (O) may be bound to the hydroxyl (-OH) groups in thioglycolic acid or from DMSO (DMSO has an S=O group). It can also be the result of slight oxidation on the surface. Nitrogen (N) may be the source of contamination during preparation or from residues of secondary compounds that appeared during the dissolution of the components. As mentioned earlier, gold (Au) is often the result of coating the sample with a thin layer to improve conductivity during analysis.

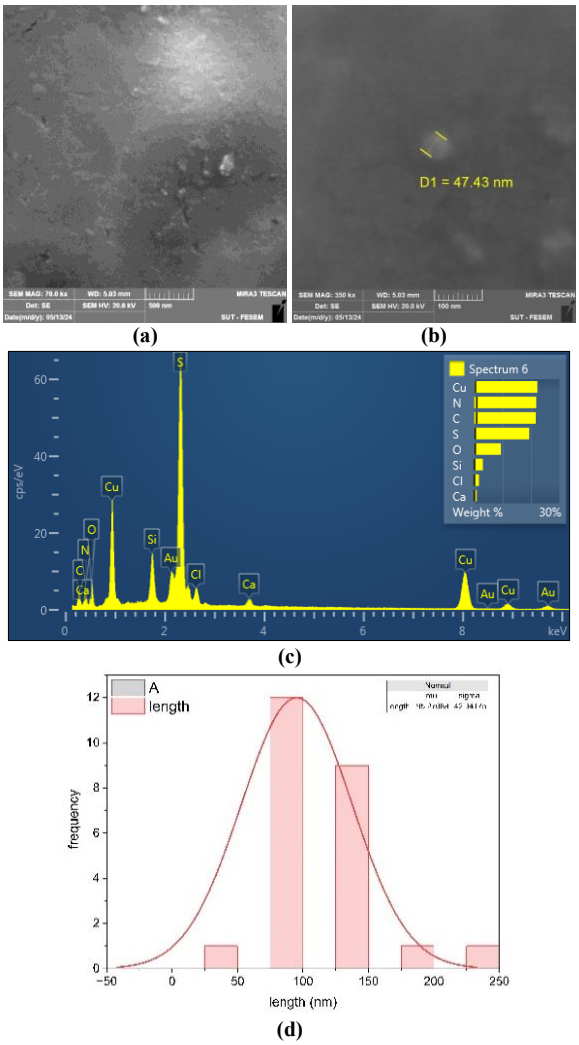

Fig. (3) FE-SEM images, EDX spectrum and particle size distribution of the $CuBiS_2$ film

Figure (4) presents a comprehensive optical characterization of $CuBiS_2$ composite thin films through various spectroscopic analyses, providing critical insights into the material's electronic structure and potential optoelectronic applications. The UV-visible absorption spectrum (Fig. 4a) contains a strong UV absorption peak centered at about 300 nm. The sharp feature may indicate a strong electronic

transition in the ultraviolet region, presumably due to the excitation of electrons from the valence band to the conduction band. The absence of any significant absorption in the visible range (400-700nm) would suggest that this material is reasonably transparent to visible light and maybe useful for specific applications in photovoltaics or photodetectors. In the plot of absorption coefficient (α) versus photon energy (Fig. 4b), an absorption edge apparently occurs around 3.75 eV, as can be seen from the steep increase in absorption at higher energies. This edge thus defines the onset of significant electronic transitions and provides a rough estimate of the material's bandgap.

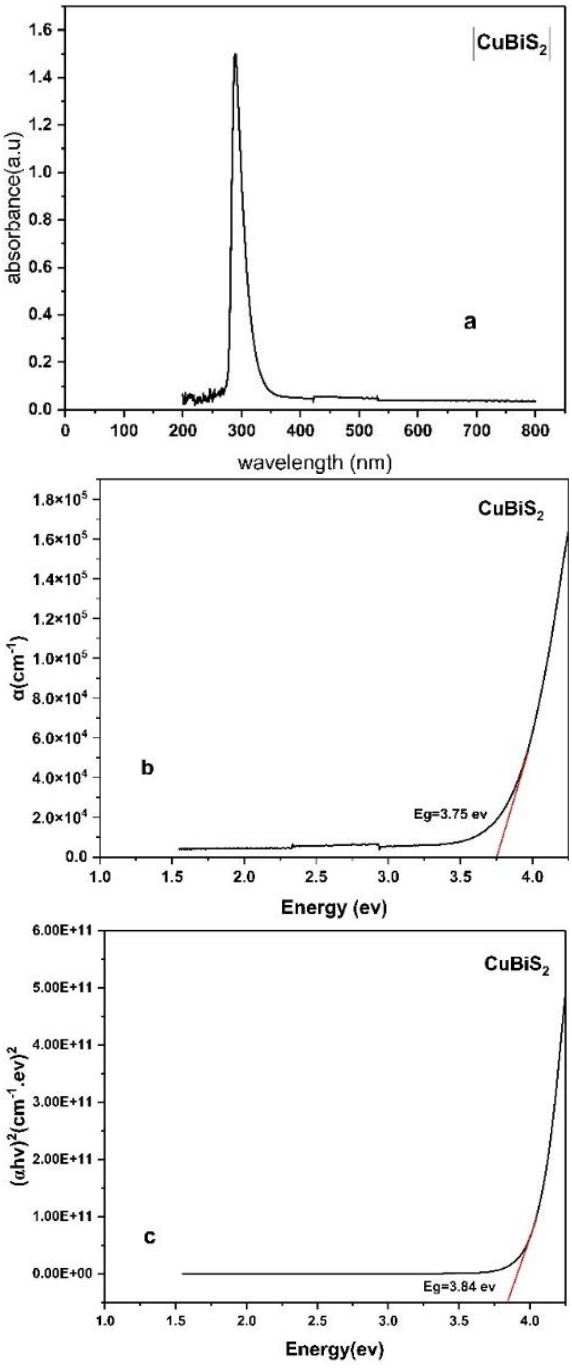

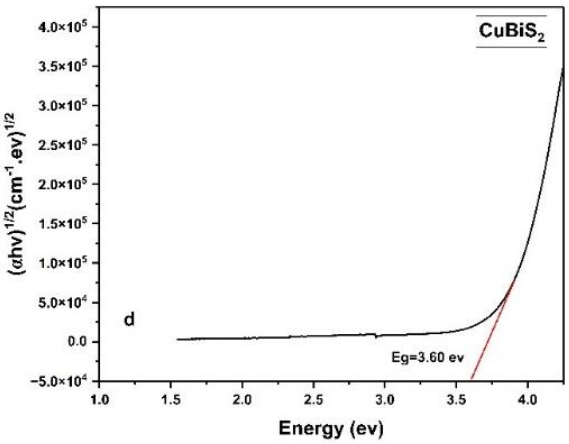

Fig. (4) Absorption spectrum and energy gap determination for the $CuBiS_2$ film prepared using thioglycolic acid

The Beer-Lambert law is used to most comprehensively describe the UV spectra relating to the nature of an electromagnetic light. The simplest form of the relevant law defining the absorbance of materials is as given in the following equation [23]

$$A = Log\left(\frac{I_0}{I}\right) = \varepsilon bc \qquad (2)$$

Here, A, I_0, I, ε, b and c refer to the absorbance of material, the intensity of the incident light, the intensity of the transmitted light, the extinction coefficient, the length of path the light passes and dose of the absorbing, respectively

The relationship between absorbance and the transmittance is presented as $A=-logT$ and $T=(I/I_0)$. In order to see the effect of material geometry on its absorption, the absorption coefficient is calculated using the absorbance values by the following equation [24]

$$\alpha = 2.303\frac{A}{t} \qquad (3)$$

In this equation, α is the absorption coefficient and t is the thickness of the tube

Tauc's plots were obtained by using the absorption coefficient values of the material. The optical energy gaps of the material were calculated using the slope of the Tauc plots, which a function of the photon energy. The relationship between the Tauc's plots and the photon energy, which allows the calculation of the forbidden energy gaps, is as in the following equation [25]

$$\alpha h\nu = B\left(h\nu - E_g\right)^n \qquad (4)$$

where, h is the Planck's constant, ν is the frequency of incident photon, B is a constant that depends on the electron mobility and the transition probability, E_g is the forbidden energy gap and n is the an index that correspond to the nature of the transition plots for direct and indirect bandgap transitions are shown in figures (4c) and (5d), respectively. Such plots are imperative to deduce the exact nature and value of the optical bandgap. The plot of $(\alpha h\nu)^2$ against photon energy, as shown in Fig. (4c), yields a bandgap value of 3.84 eV for direct transitions. Figure (4d) shows the

plot of $(\alpha h\nu)^{½}$ vs photon energy, which is indicative of an indirect bandgap of 3.60 eV. Since both direct and indirect bandgap characteristics were observed, the band structure in $CuBiS_2$ would then be complicated.

The obtained direct bandgap of 3.84 eV suggests an efficient light absorption and thus a strong photoluminescence which might be an important parameter for optoelectronic devices. The relatively lower indirect bandgap of 3.60 eV would enhance the charge carrier lifetime, hence being useful in photovoltaic applications. Wide-bandgap material above 3.5 eV classifies $CuBiS_2$ as promising toward ultraviolet optoelectronics. This allows for UV photodetectors, transparent conductors, or application as a window layer in multi-junction solar cells. The fact that bandgap values obtained through different methods - AE and plots - show slight differences underlines the necessity for complete optical characterization of the films. It is obvious that these measurements could be influenced by film thickness, surface roughness, and defect states; hence, one must be very cautious with interpretation. To summarize, the investigated optical properties of $CuBiS_2$ composite thin films point out the wide-bandgap semiconductor behavior with both direct and indirect transition characteristics. Such findings, on one side, explain the basic electronic structure of the material; on the other side, they point out the potential applications in several optoelectronic applications, particularly those working in the ultraviolet range. Other studies that relate such optical properties with structural and electrical features of the material would be useful in the view of performance optimization in specific device architectures.

Tables (3) and (4) represent some of the essential electrical characterizations of $CuBiS_2$ composite thin films and give useful information about transport properties and temperature variation in the composites. Table (3) summarizes Hall effect measurement results with some associated electrical parameters. The Hall mobility lies in the range 1.15×10^{2}-2.13×10^{2} $cm^2/V\cdot s$, which reflects mediocre charge carrier mobility in the material. This conductivity range suggests that, though carriers are mobile, some scattering mechanisms are involved and could be due to the presence of grain boundaries or some sort of defects in the thin film structure. Values of conductivity measured at around 2.3×10^{-5} S/cm reveal that the CuBiS2 films are semiconductor materials. Similarly, the corresponding resistivity values, around 4.2×10^{4}-4.4×10^{4} $\Omega\cdot cm$, further confirm its nature as semiconducting material. These values are representative for a lot of chalcogenide semiconductors and indicate possible applications in thermoelectric devices or as an absorber layer in photovoltaic cells. The Hall coefficient, in the range of 4.82×10^{6} to 9.30×10^{6} cm^3/C, provides information on the prevailing charge carriers. Positive values confirm holes as the majority carriers; hence, $CuBiS_2$ is classified as a p-type semiconductor in this configuration. It is either intrinsic to the material or induced by specific growth conditions or by defect chemistry. Data in table (3) are used to analyze temperature dependence of conductivity as an Arrhenius plot. The nominal temperature of 301 K for all measurements means that the analysis concerns the properties at room temperature. The plot of $\ln(\sigma_{dc})$ as a function of 1000/T will enable us to extract the activation energy for conduction, the most important parameter for the understanding of thermal activation of charge carriers. These small variations of conductivity values, from 2.29×10^{-5} to 2.39×10^{-5} S/cm at the same temperature, with their respective $\ln(\sigma)$ values varying between -10.68 and -10.64, reflect small fluctuations in the measurement or sample, indicating very good reproducibility in the electrical properties. The contents provided in these electrical characterizations are the bases for beginning an understanding of the charge transport mechanism in $CuBiS_2$ composite thin films. Moderate values of mobility and conductivity, besides p-type conductivity, make these films promising for applications involving controlled hole conduction. Further studies on the temperature dependence of these properties over a wider range would be useful in elucidating the activation energies and multiple mechanisms of conduction operating in these materials..

The electron mobility is defined by the equation [26]:

$$\upsilon_d=\mu_h E \quad (3)$$

The detailed analysis on the gas sensing characteristics of $CuBiS_2$ composite thin films including their response to H_2S gas at different temperatures is given in Fig. (5) and table (5). This data is important in understanding the utilization possibilities of the material as a gas sensing element. Figures (5a) and (5b) represents the dynamic resistance changes of $CuBiS_2$ film in the presence of H_2S vapor at 100°C and 140°C, respectively. Maximum resistance is observed upon gas exposure (gas on phase). A decrease in resistance is observed on cessation of the gas flow (gas off phase). Such behavior is typical of p-type semiconductor materials in the presence of reducing gases like H_2S. The presence of greater resistance change at 140°C suggests better sensitivity at higher temperatures. Figures (5c) and (5d) depict the temperature dependence of sensor response and recovery time respectively. The response time increased, from 18.9 seconds at 100°C to 23.4 s at 140°C. This points to the time taken by the sensor to respond to gas presence. The graph aligns with the expected response time where malign within the typical range of a gas sensor in the presence of H_2S gas at $CuBiS_2$. Conversely, recovery time decreased from 81.9 s at 100°C to 45.9 s at 140°C.

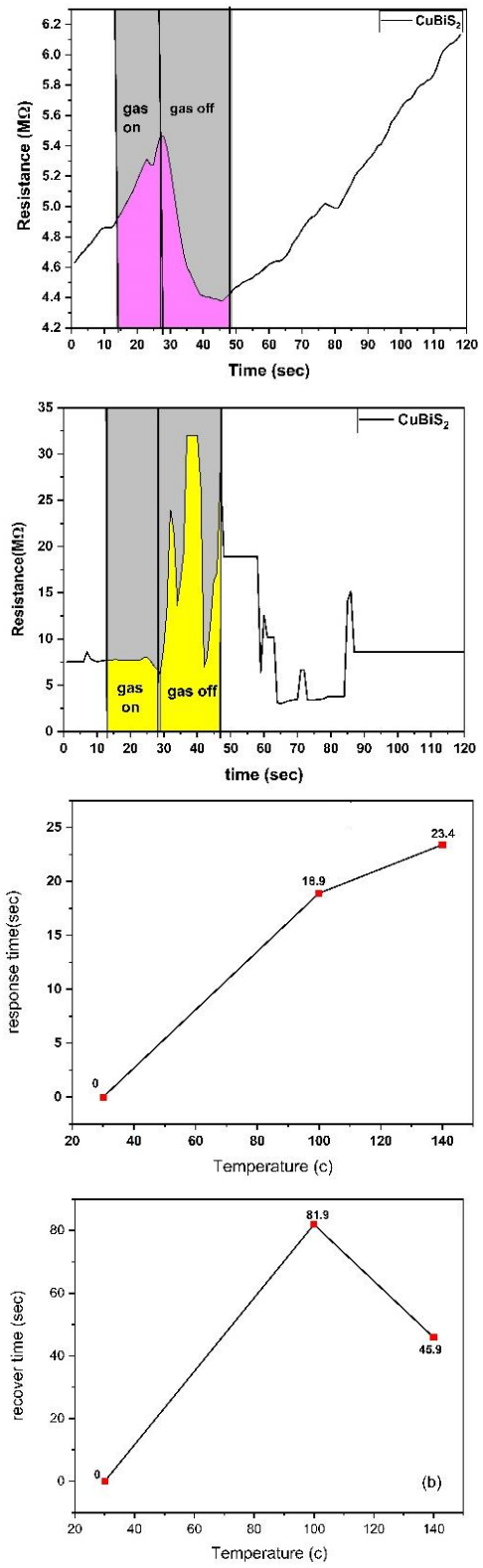

Fig. (5) Temperature-dependent resistance dynamics of $CuBiS_2$ film prepared using Thioglycolic acid under H_2S gas exposure and removal cycles at three distinct temperatures (a) 100°C, (b) 140°C and depict the temperature dependence of sensor (c) response time (d) recovery time

Recovery time represents time taken to return to the baseline after exposure. This trend suggests that while higher temperatures slightly slow the initial response, they greatly accelerate the sensor's recovery process. Table (5) provides quantitative data on the sensor's performance across different temperatures. The sensitivity, calculated as the ratio of resistance change to initial resistance, shows a remarkable increase from 23.53% at 100°C to 59.33% at 140°C. This substantial improvement in sensitivity with temperature indicates that the gas-surface interactions become more favorable at higher temperatures, likely due to enhanced adsorption and desorption kinetics. The absence of data at 30°C (marked with zeros in the table) suggests that the sensor may not be effective at room temperature, highlighting the importance of operating these $CuBiS_2$-based sensors at elevated temperatures for optimal performance. The significant increase in both R_{on} and R_{off} values from 100°C to 140°C, coupled with the enhanced sensitivity, demonstrates that temperature plays a crucial role in modulating the sensor's electrical properties and its interaction with H_2S gas. This analysis has thus shown that composite $CuBiS_2$ thin films possess promising characteristics as H_2S gas sensors, whose performance optimizes at higher temperatures. At 140°C, the material possesses a good balance of sensitivity and response/recovery times and is hence a good candidate for applications that require fast and sensitive detection of H_2S gas. Further optimization of the operating temperature is a future direction of work, together with investigation of the sensor's selectivity towards other gases in view of widening its perspectives for application in environmental monitoring and industrial safety.

Figure (6) and table (6) summarize a detailed approach toward the NO_2 gas sensing properties of composite $CuBiS_2$ thin films at three different temperatures, providing good background on the capability of the material to act as a gas sensing element for oxidizing gases. Figures (7a) and (7b) present the dynamic resistance change of the $CuBiS_2$ film when exposed to NO_2 gas at 100°C and 140°C, respectively. Contrary to that, in the case of H_2S, the resistance increases upon NO_2 exposure and is in good agreement with the behavior caused by the interaction of p-type semiconductors with oxidizing gases. The resistance change is more pronounced at 140°C, suggesting enhanced sensitivity at higher temperatures. The temperature dependence of the sensor's response and recovery times is depicted in figures (6c) and (6d). Interestingly, the response time increases from 9 s at 100°C to 20.7 s at 140°C, indicating a slower initial response at higher temperatures The recovery time, however, decreases from 61.2 s at 100°C to 45.9 s at 140°C, demonstrating faster sensor regeneration at elevated temperatures.

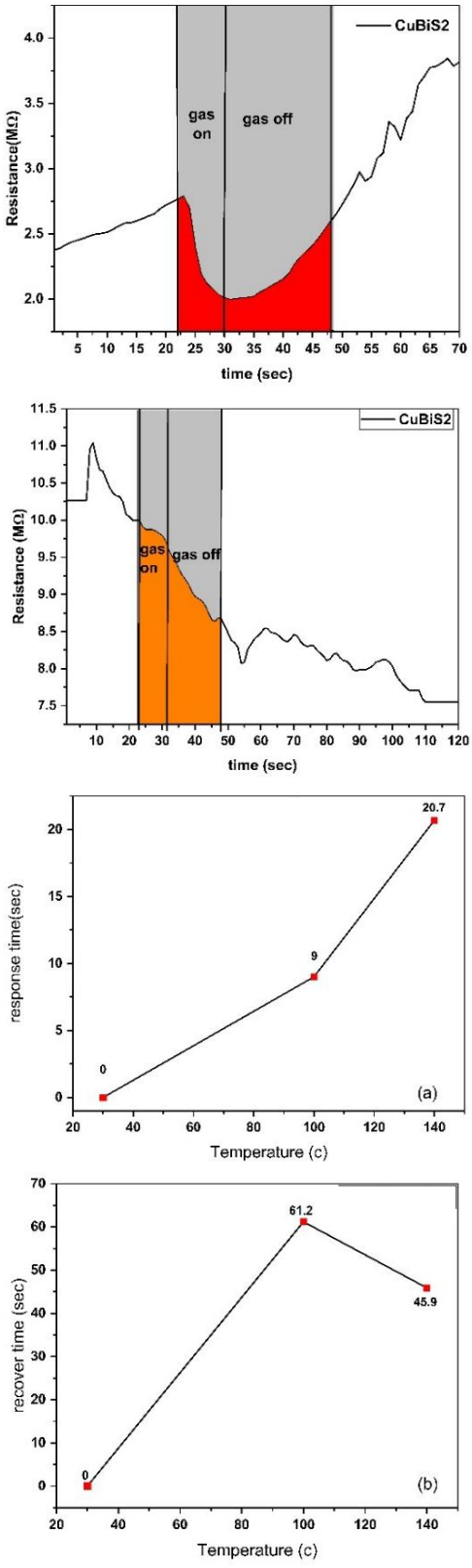

Fig. (6) Temperature-dependent resistance dynamics of $CuBiS_2$ film prepared using Thioglycolic acid under NO_2 gas exposure and removal cycles at three distinct temperatures (a) 100°C, (b) 140°C and depict the temperature dependence of sensor (c) response time (d) recovery time

Table (7) quantifies the sensor's performance across different temperatures. The sensitivity, calculated as the percentage change in resistance, shows an unexpected trend. It decreases from 38.08% at 100°C to 15.03% at 140°C, contrary to the behavior observed with H_2S. This suggests that the interaction mechanism between NO_2 and the $CuBiS_2$ surface may be more complex and temperature-dependent than for H_2S. The absence of data at 30°C (marked with zeros in the table) implies that the sensor may not be effective for NO_2 detection at room temperature, emphasizing the necessity of elevated operating temperatures for optimal performance. The increase in both R_{on} and R_{off} values from 100°C to 140°C indicates that temperature significantly influences the film's electrical properties. However, the smaller relative difference between R_{on} and R_{off} at 140°C explains the reduced sensitivity at this temperature.

Therefore, this analysis points out that composite $CuBiS_2$ thin films present different sensing characteristics for both NO_2 and H_2S. Moreover, whereas the sensor exhibited higher sensitivity at 100°C for NO_2, recovery occurred at a faster rate at 140°C. Such temperature-dependent behavior is indicative of optimization of operating temperature.

The responsivity and response time are respectively defined here as [27]:

$$S_{res} = \frac{|R1-R2|}{R2} \quad (4)$$

$$\tau_{res} = t_2 - t_1 \quad (5)$$

The contrastive trends for NO_2 and H_2S testify to the great potential of $CuBiS_2$ thin films in developing selective gas sensors. Further studies may be devoted to a deeper understanding of the mechanisms of gas-surface interaction at different temperatures, and then sensor performance with gas mixtures should be probed for the goal of improving selectivity and practical applicability in both environmental monitoring and industrial safety.

4. Conclusion

The CuBiS2 composite thin films showed promising gas sensing for both H_2S and NO_2 gases, with temperature dependence of response and recovery times. For each gas, the temperature of operation that provided an optimal compromise in sensitivity and response time was determined. The observed selectivity between reducing and oxidizing gases, specifically H_2S and NO_2, respectively, paves the way for the development of multi-gas sensors based on this material. Further refinement of the composition and structure of the films to improve sensitivity and selectivity, along with the evaluation of sensing performance for other gases of environmental and industrial relevance, will be the focus of subsequent investigations. This research contributes significantly to the rapidly advancing field of nanostructured materials for gas sensing applications

and offers pathways for the development of efficient, cost-effective, and reliable gas sensors based on $CuBiS_2$ composite thin films.

References

[1] S. Carli et al., "Single walled carbon nanohorns composite for neural sensing and stimulation", *Sens. Actuat. B: Chem*, 271 (2018) 280–288.

[2] J. Lee et al., "Interplay between Short- and Long-Ranged Forces Leading to the Formation of Ag Nanoparticle Superlattice", *Small*, 15(33) (2019) 01966.

[3] S.V. Pershina et al., "Glass-ceramics in $Li_{1+x}Al_xGe_{2-x}(PO_4)_3$ system: The effect of Al_2O_3 addition on microstructure, structure and electrical properties", *J. Alloys Comp.*, 835 (2020) 155281.

[4] R.G. Balakrishna, "Ratiometric probe of PQDs/R6G: Achieving high sensitivity and precision in contaminant detection", *Sens. Actuat. B: Chem.*, 397 (2023) 134626.

[5] Y. Liu et al., "Highly selective and sensitive fluorescence detection of hydroquinone using novel silicon quantum dots", *Sens. Actuat. B: Chem.*, 275 (2018) 415–421.

[6] S. Boudinar et al., "Electrochemical nucleation and optical characterization of highly oriented Bi clusters on Cu substrate", *Thin Solid Films*, 684 (2019) 68–77.

[7] H. Deng et al., "Progress on the morphological control of conductive network in conductive polymer composites and the use as electroactive multifunctional materials", *Prog. Polym. Sci.*, 39(4) (2014) 627–655.

[8] F.E. Loranca-Ramos et al., "Structural, optical and electrical properties of copper antimony sulfide thin films grown by a citrate-assisted single chemical bath deposition", *Appl. Surf. Sci.*, 427 (2018) 1099–1106.

[9] G. Di et al., "Visible-light degradation of sulfonamides by Z-scheme $ZnO/g\text{-}C_3N_4$ heterojunctions with amorphous Fe_2O_3 as electron mediator", *J. Colloid. Interface. Sci.*, 538 (2019) 256–266.

[10] M.S. Libório et al., "A Review of Cu_3BiS_3 Thin Films: A Sustainable and Cost-Effective Photovoltaic Material", *Crystals*, 14(6) (2024) 524.

[11] M. Zhu et al., "Prussian blue nanocubes supported on graphene foam as superior binder-free anode of lithium-ion batteries", *J. Alloys Comp.*, 749 (2018) 811–817.

[12] R. Jana et al., "Recent advances in multifunctional materials for gas sensing applications", *J. Enviro. Chem. Eng.*, 10(6) (2022) 108543.

[13] F. Bai et al., "Lead-free, air-stable ultrathin $Cs_3Bi_2I_9$ perovskite nanosheets for solar cells", *Solar Ener. Mater. Solar Cells*, 184 (2018) 15-21.

[14] F. Della Pelle et al., "High-performance carbon black/molybdenum disulfide nanohybrid sensor for cocoa catechins determination using an extraction-free approach", *Sens. Actuat. B: Chem.*, 296 (2019) 126651.

[15] B. Khodadadi et al., "Green synthesis of Ag nanoparticles/clinoptilolite using Vaccinium macrocarpon fruit extract and its excellent catalytic activity for reduction of organic dyes", *J. Alloys Comp.*, 719 (2017) 82-88.

[16] M.A. Khan et al., "Recent Trends in Electrochemical Detection of NH_3, H_2S and NO_x Gases", *Int. J. Electrochem. Sci.*, 12(3) (2017) 1711-1733.

[17] A. Giaccherini et al., "Thermochemistry of the E-ALD process for the growth of Cu_xZn_yS on Ag(111): Interpretation of experimental data", *Electrochim. Acta*, 262 (2018) 135–143.

[18] V. Goulart Isoppo et al., "Highly fluorescent lipophilic 2,1,3-benzothiadiazole fluorophores as optical sensors for tagging material and gasoline adulteration with ethanol", *Sens. Actuat. B: Chem.*, 309 (2020) 127701.

[19] L. Xu et al., "Interactions between a polymer electrolyte membrane fuel cell and boost converter utilizing a multiscale model", *J. Power Sources.*, 395 (2018) 237-250.

[20] M. Qader Kareem, S. Abd-allah Hassan and M. Mohammed Ameen, "Doping Effect ($(COCl_2.6H_2O)$ & $(CuCl_2.6H_2O)$) (2%)w/v on Optical Energy gap of (GA/PVA) composite films", *Tikrit J. Pure Sci.*, 20(4) (2015) 114-119.

[21] M.Q. Kareem et al., "Synthesis of Tetrahedrite Zincian Nanocomposites via solvothermal process at low temperature", *Ceram. Int.*, 50(20) (2024) 40005-40013.

[22] V.A. Johnson and K. Lark-Horovitz, **"Solid State Physics, Part A : Preparation, Structure, Mechanical and Thermal Properties"**, Academic Press (NY, 1959) p. 483.

[23] M. Öztürk, "Determination of Quality in Homemade Vinegars by Spectroscopy and Rheology Methods", *Düzce Univ. J. Sci. Technol.,* 9(4) (2021) 1493–1506.

[24] C. Dishovsky, A. Pivovarov and H. Benschop (eds.), **"Medical treatment of intoxications and decontamination of chemical agents in the area of terrorist attack"**, Springer (2006), p. 233.

[25] R. Saravanan, **"Solid oxide fuel cell (SOFC) materials"**, Materials Research Forum, L.L.C. (PA, 2018), p. 171.

[26] J. Jerhot and V. Šnejdar, "Hall effect in polycrystalline semiconductors", *Thin Solid Films*, 52(3) (1978) 379–395.

[27] W.J. van der Linden and R.K. Hambleton, **"Handbook of Modern Item Response Theory"**, Springer (NY, 2013) p. 30.

Table (1) Comparative XRD data and structural information for $CuBiS_2$

2θ (deg)	FWHM (deg)	d_{xrd} (Å)	d_{JCPDS} (Å)	Intensity (%)	hkl	Crystal system	Card NO.
15.428	2.1273	3.27256	3.25000	40.0	(3,1,0)	Monoclinic	00-008-0086
19.984	1.3287	3.05792	3.07000	100	(-3,1,2)		
23.582	1.1625	2.80225	2.86000	5.0	(-3,1,3)		
28.697	1.9548	3.10468	1.87700	5.0	(-3,1,7)		

Table (2) Key features observed in the FTIR spectrum of $CuBiS_2$ composite thin films

Wavenumber (cm^{-1})	Peak Intensity	Possible Assignment
3867	weak	O-H stretching (free or non-hydrogen bonded)
3749	weak	O-H stretching (isolated)
3376	Strong, Broad	O-H stretching (hydrogen bonded)
1668	Medium	H-O-H bending (water molecules)
1424	weak	C-H bending (possible organic residues)
1014	strong	S-O stretching (surface oxidation)
664	Strong , sharp	M-S stretching (Cu-S and Bi-S bonds)

Table (3) Data related to Hall effect, temperature, conductivity, resistivity, mobility, current, and Hall coefficient

Temperature (°C)	Current (A)	Resistivity (Ω.cm)	Conductivity $(\Omega.cm)^{-1}$	Mobility ($cm^2/V.s$)	Hall Coefficient (average) (cm^3/C)
28	5.00E-09	4.37E+04	2.29E-05	2.13E+02	9.30E+06
28	5.00E-09	4.18E+04	2.39E-05	1.53E+02	6.39E+06
28	5.00E-09	4.18E+04	2.39E-05	1.15E+02	4.82E+06

Table (4) Temperature-dependent DC conductivity

Temperature (°C)	Conductivity (σ) $(\Omega.cm)^{-1}$	1000/T	Ln(σ)
28	2.29E-05	3.32226	-10.68437
28	2.39E-05	3.32226	-10.64163
28	2.39E-05	3.32226	-10.64163

Table (5) Temperature-dependent performance metrics of $CuBiS_2$ film gas sensor for H_2S

Temperature (°C)	Time on	Time of	R_{on}	R_{off}	Recovery Time (s)	Response Time (s)	Sensitivity (%)
30	0	0	0	0	0	0	0
100	28	49	5.46	4.42	81.9	18.9	23.53
140	23	49	7.69	18.91	45.9	23.4	59.33

Table (6) Temperature-dependent performance metrics of $CuBiS_2$ film gas sensor for NO_2

Temperature (°C)	Time on	Time of	R_{on}	R_{off}	Recovery Time (s)	Response Time (s)	Sensitivity (%)
30	0	0	0	0	0	0	0
100	22	32	2.763	2.001	61.2	9	38.08
140	26	49	9.87	8.58	45.9	20.7	15.03

